Quantum measurement spintronic engine powered by quantum coherence enhanced by bosonic catalysis

Mathieu Lamblin* and Martin Bowen†
Institut de Physique et Chimie des Matériaux de Strasbourg, UMR 7504 CNRS, Université de Strasbourg, 23 Rue du Læss, BP 43, 67034 Strasbourg, France

(Received 27 July 2023; accepted 15 March 2024; published 12 April 2024)

Quantum information engines can advantageously convert information into work, usually through a feedback mechanism operated by a Maxwell demon. In principle, this opens prospects of autonomous machines that challenge the classical second law of thermodynamics. Yet prior research, which typically tests a given concept in isolation, usually makes strong assumptions on turning on/off internal interactions or the connection to the baths, which has fueled skepticism. Meanwhile, several recent experiments describe an autonomous spintronic engine that purportedly combines several concepts using inherent electronic interactions to harvest spin fluctuations and quantum correlations. So far, no full-fledged theory has described it. In this article, we address these several interdisciplinary shortcomings by presenting a theory for a solid-state, fully electronic spintronic quantum information engine that converts the energy of quantum coherence into useful electrical work thanks to quantum measurements. Our simple two-stroke engine operates on two correlated atomic, single-spin quantum dots (QDs) that are connected in series with two ferromagnetic electrodes. The ultrafast measurement stroke destroys the quantum coherence stored within the QDs and projects the system into a local high-energy separated state. The resulting energy is then released into the leads as electrical current when the partial thermalizing stroke restores quantum coherence. Using a master equation approach, we show that a robust steady-state current can flow between the electrodes despite the absence of a tunneling path and at thermal equilibrium. Our model proves the feasibility of harvesting quantum fluctuations by the measurement back-action through the on-site Coulomb interaction, and can reproduce experimental output power levels if bosons mediate this transport in the presence of an additional nonequilibrium resource. This can for instance be accomplished by the spin bias that is inherently generated by the ferromagnetic electrodes. Our work raises the prospect of measuring the "spintronic temperature" of the leads using magnetization dynamics experiments, while the model's underpinnings of built-in, materials-inherent measurements of quantum information can in principle be adapted to describe fundamental quantum processes in chemistry and biology.

DOI: 10.1103/PhysRevB.109.165423

I. INTRODUCTION

The emerging field of quantum thermodynamics [1], specifically of quantum energetics [2], has researched quantum thermal machines and quantum batteries [3] in the hope of finding new ways of producing energy at the nanoscale. A first approach describes quantum analogs to classical engines that rely either on Maxwell's demon [4,5], a cycle between different baths [6–8], or an external drive [9–11]. A second approach focuses on systems that specifically rely on quantum features such as coherence [12–15] and entanglement [16–18] in order to extract energy from the environment using the singular properties of quantum superposition and quantum measurements. These new kinds of quantum engines, which have been demonstrated experimentally [19–23], redefine the notion of temperature when examining engine efficiencies against the Carnot limit [7,24–26], notably when harvesting energy from a single heat bath [27,28].

Quantum measurements constitute a critical process that could lead to active devices that use coherence as a fuel [29,30]. Indeed, the resulting projection that such a measurement performs on a quantum state involves an irreversible energy exchange between the state and the environment [2] that can be viewed as a form of quantum heat [31]. The information obtained from the measurement can either be used by a Maxwell demon [17,31] that can extract energy by applying some unitary transformation to the working substance (WS), or the measurement back-action itself can result in an energy increase that can be harvested into useful work [28].

In these engine models, the proposed cycle is not autonomous and can be difficult to implement experimentally [13,14,18,24], while the practical cost of turning on/off interactions within the system [18] or between the WS and the baths [6–8,24,26,32] is ignored. In this article, we model a quantum electronic engine that mostly lifts these limitations. Frequent quantum measurements that are inherent to the electronic steady state provide energy to the WS, part of which is then released to the external circuit in the form of electrical work when the system relaxes to the equilibrium state. The

*mathieu.lamblin@ipcms.unistra.fr
†bowen@unistra.fr

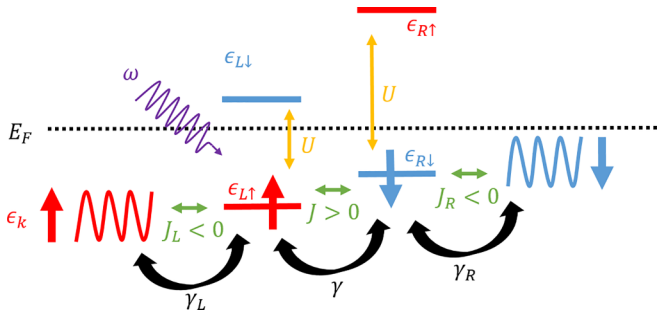

FIG. 1. Illustration of the model quantum spintronic engine, featuring two quantum dots trapped in series between two ferromagnetic leads in an antiparallel configuration with fully spin-polarized interactions. Blue/red levels represent spin ↓/↑ energy levels. Green double arrows represent the magnetic couplings; yellow double arrows, capacitive couplings; and black arrows, tunnel couplings.

device promotes quantum fluctuations in the sense that it favors the emergence of a current in a system featuring no direct tunneling link between the two leads and connected to an environment with no out-of-equilibrium properties. Strikingly, we also show that it advantageously mimics a recent yet unexplained experimental implementation [19,20] with a comparable power output if a bosonic bath is included along with an out-of-equilibrium hypothesis.

We build upon the initial formalism [33–35] used to phenomenologically model magnetotransport across the spintronic device under the assumption of effective work [19]. This article is a first step towards removing this assumption and describing this class of spintronic devices within a broader quantum thermodynamical framework. We pedagogically describe the several concepts and interactions for our autonomous solid-state spintronic engine hereafter, while calculations are shown in the Supplemental Material [36].

II. MODEL

A. Hamiltonian

1. General Hamiltonian

In this article, we consider two quantum dots (QDs). Each QD, or atomic dot, consists of two nondegenerate electronic energy levels that code for two opposite spins on the Bloch sphere. The two QDs are coupled with one another by a tunneling interaction of magnitude γ and a magnetic exchange interaction of magnitude J. A Coulombic repulsion term U is also considered so as to prevent excessive charging on each dot. The environment is composed of two ferromagnetic leads, the left one L and the right one R, each of them respectively coupled to the left and right QDs. From these elements, the total Hamiltonian H can be separated as

$$H = H_S + H_E + H_{SE}. \tag{1}$$

The first term H_S, called the Hamiltonian of the system, represents the two spin qubits and can be written as (see Fig. 1)

$$\begin{aligned} H_S = {} & \epsilon_{L\uparrow} n_{L\uparrow} + \epsilon_{L\downarrow} n_{L\downarrow} + \epsilon_{R\uparrow} n_{R\uparrow} + \epsilon_{R\downarrow} n_{R\downarrow} \\ & + \gamma c_{L\uparrow}^\dagger c_{R\uparrow} + \gamma^* c_{L\uparrow} c_{R\uparrow}^\dagger + \gamma c_{L\downarrow}^\dagger c_{R\downarrow} + \gamma^* c_{L\downarrow} c_{R\downarrow}^\dagger \\ & - U[(1-n_{L\uparrow})n_{L\downarrow} + n_{L\uparrow}(1-n_{L\downarrow})] \\ & - U[(1-n_{R\uparrow})n_{R\downarrow} + n_{R\uparrow}(1-n_{R\downarrow})] \\ & - J(n_{L\uparrow}n_{R\uparrow} + n_{L\downarrow}n_{R\downarrow}), \end{aligned} \tag{2}$$

where we have defined $c^\dagger$ and c as the raising and lowering operators with the left index identifying the left or right quantum dot and the right index identifying the spin. The n correspond to the number operators defined as $n = c^\dagger c$. Let us explain the physical meaning of those terms. The first terms in ϵ correspond to the bare energy of each of the four electrons that can occupy the two quantum dots. We assume that the energies ϵ are different for each level and we will see below that their relative values can be tuned through the couplings.

The terms in γ code for the hopping electron transmission between the QDs. The spin is preserved during this transfer as no spin flip is possible during the hopping to leading order. The electron hopping argument γ is taken as independent of the tunneling spin for simplicity. Although this tunneling argument should strongly depend on the considered spin channel given the spin splitting of the energy level, this assumption is not critical here given the approximations we make later.

The terms in J represent the magnetic coupling between the two quantum dots. Since prior literature indicates antiferromagnetic coupling and spontaneous current flow at $V = 0$ [19,20], we therefore assume that $J < 0$. As we can see, this contribution adds an energy penalty of $-J$ when an electron of the same spin is present on both QDs. This repulsion term J is considered independent of the spin orientation for simplicity, and we will see in the following that this approximation holds given the weak relevance of J in the next results.

Finally, the terms in U correspond to the Coulombic repulsion, which lowers the energy when a quantum dot is singly occupied. The term has been included to avoid excessive charge being retained on the system. We assume that this Coulomb repulsion energy is identical on the two sites.

This Hamiltonian can be simplified by rescaling the energies. Redefining $\epsilon \equiv \epsilon - U$ and $U \equiv U/2$, we get

$$\begin{aligned} H_S = {} & \epsilon_{L\uparrow} n_{L\uparrow} + \epsilon_{L\downarrow} n_{L\downarrow} + \epsilon_{R\uparrow} n_{R\uparrow} + \epsilon_{R\downarrow} n_{R\downarrow} \\ & + \gamma c_{L\uparrow}^\dagger c_{R\uparrow} + \gamma^* c_{L\uparrow} c_{R\uparrow}^\dagger + \gamma c_{L\downarrow}^\dagger c_{R\downarrow} + \gamma^* c_{L\downarrow} c_{R\downarrow}^\dagger \\ & - J(n_{L\uparrow}n_{R\uparrow} + n_{L\downarrow}n_{R\downarrow}) + U(n_{L\uparrow}n_{L\downarrow} + n_{R\uparrow}n_{R\downarrow}). \end{aligned} \tag{3}$$

The second contribution to the Hamiltonian describes the energy of the ferromagnetic reservoirs, i.e., the environment of the QDs. It can be split into two terms $H_E = H_L + H_R$ describing each electrode:

$$H_L = \sum_{k\sigma} \epsilon_{k\sigma}\, c_{k\sigma}^\dagger c_{k\sigma}, \; H_R = \sum_{p\sigma} \epsilon_{p\sigma}\, c_{p\sigma}^\dagger c_{p\sigma}, \tag{4}$$

where the index σ accounts for the spin degrees of freedom while the indexes k and p are used for the left (L) and right (R) leads, such that $\epsilon_{k,\sigma}$ and $\epsilon_{p,\sigma}$ are the energies of each fermionic mode of the field while $c_{k,\sigma}^\dagger$, $c_{p,\sigma}^\dagger$, $c_{k,\sigma}$, and $c_{p,\sigma}$ are the creation and annihilation operators. Only a single band is considered on each lead. This hypothesis is in line with a description of dominant transmission from a specific wave function in most tunneling spintronic devices [37]. It is especially valid given prior experiments [19,20] on the quantum spintronic engine that utilize the ferromagnetic

metal/molecule interface (i.e., the spinterface [38,39]) to generate electrodes with a spectrally narrow band of conduction states with full spin polarization.

The final term H_{SE} describes the tunneling interaction between the system (i.e., the QDs) and the environment (i.e., the leads). This term can also be split into two parts $H_{SE} = H_{SL} + H_{SR}$. For each lead, we consider two contributions. The first contribution describes the exchange of electrons between the lead and the system, more precisely the adjacent QD since we consider a series geometry. This allows for a current to emerge in the model. The second contribution describes the magnetic pinning exerted by the lead on the nearby site to model the effective magnetic field generated by spintronic anisotropy [19,20,40]. Following these assumptions, we get

$$H_{SL} = \sum_{k\sigma} \gamma_{k\sigma}\, c^{\dagger}_{L\sigma} c_{k\sigma} + \gamma_{k\sigma} * c_{L\sigma} c^{\dagger}_{k\sigma} + J_{k\sigma}\, n_{L\sigma} n_{k\sigma},$$

$$H_{SR} = \sum_{p\sigma} \gamma_{p\sigma}\, c^{\dagger}_{R\sigma} c_{p\sigma} + \gamma_{p\sigma} * c_{R\sigma} c^{\dagger}_{p\sigma} + J_{p\sigma}\, n_{R\sigma} n_{p\sigma}.$$

The coefficients γ represent the hopping coefficients between the QDs and the electrodes, while the J represent the magnetic coupling. Note that our Hamiltonian does not describe an external bias voltage applied across the device: we are considering the case of spontaneous current flow.

2. Primary approximations

The Hamiltonian we are considering is too complex to be tackled as such analytically. We therefore physically justify the three following approximations.

First, the spinterface present in experimental devices generates conduction electrons of only one spin that, furthermore, are fixed on the Bloch sphere due to the remanent magnetization of the ferromagnetic electrode underscoring this interfacial effect [20]. Furthermore, experiments indicate better current output when the device's electrode magnetizations are oriented antiparallel. As a result, assuming identical left and right interfaces, we will consider only spin ↑ electrons in the left lead and spin ↓ electrons in the right lead. This consideration leads to an approximation of the electrodes and the tunnel Hamiltonians such that

$$H_L = \sum_k \epsilon_k\, c^{\dagger}_k c_k,\ H_R = \sum_p \epsilon_p\, c^{\dagger}_p c_p, \tag{5}$$

and

$$H_{SL} = \sum_k (\gamma_k\, c^{\dagger}_{L\uparrow} c_k + \gamma_k * c_{L\uparrow} c^{\dagger}_k) + \sum_k J_k\, n_{L\uparrow} n_k,$$

$$H_{SR} = \sum_p (\gamma_p\, c^{\dagger}_{R\downarrow} c_p + \gamma_p * c_{R\downarrow} c^{\dagger}_p) + \sum_p J_p\, n_{R\downarrow} n_p. \tag{6}$$

It should be pointed out that $c^{\dagger}_k$ creates an excitation with spin ↑ and momentum k in the left lead, while $c^{\dagger}_p$ creates an excitation of spin ↓ and momentum p in the right lead.

Our second assumption is that the effective magnetic field generated through spintronic anisotropy by the fully spin-polarized transport from a lead onto the adjacent QD is constant. This holds at constant bias voltage [19], consistently with the absence of an applied bias in our model. This is also reasonable to first order during engine operation given the much lower formation energy of the ferromagnetic state relative to the engine energies, owing in part to a much larger size compared to that of the atomic dots. We therefore rely on a mean field approach, which allows us to approximate the magnetic couplings as

$$\sum_k J_k n_k = \left\langle \sum_k J_k n_k \right\rangle \equiv J_L,\ \sum_p J_p n_p = \left\langle \sum_p J_p n_p \right\rangle \equiv J_R. \tag{7}$$

This approximation allows us to omit the magnetic coupling term in the system-lead interaction and add it to the system Hamiltonian without changing its structure by rescaling the QDs' energy level. Redefining $\epsilon_{L\uparrow} \equiv \epsilon_{L\uparrow} + J_L$ and $\epsilon_{R\downarrow} \equiv \epsilon_{R\downarrow} + J_R$, the system Hamiltonian remains unchanged and the tunnel Hamiltonian now reads

$$H_{SL} = \sum_k (\gamma_k\, c^{\dagger}_{L\uparrow} c_k + \gamma_k * c_{L\uparrow} c^{\dagger}_k),$$

$$H_{SR} = \sum_p (\gamma_p\, c^{\dagger}_{R\downarrow} c_p + \gamma_p * c_{R\downarrow} c^{\dagger}_p). \tag{8}$$

Finally, the quantum spintronic engine concept as proposed [19,20] includes an asymmetry in the tunneling coefficients γ_L and γ_R. This not only helps to further break detailed balance of transport, but also enables one electrode to set a dominant spin referential on the QDs. As a result, the QD that is adjacent to that electrode will experience a larger spin splitting than the other QD. Therefore, we assume that the right QD is positioned such that $\epsilon_{R\uparrow} \gg \epsilon_{R\downarrow}, \epsilon_{L\uparrow}, \epsilon_{L\downarrow}$. Placing this energy level farther above the other ones allows us to discard all the states where a spin ↑ occupies the right QD, thereby reducing the dimensionality of the system Hamiltonian from 16 down to 8:

$$H_S = \epsilon_{\uparrow} n_{\uparrow} + \epsilon_{\downarrow} n_{\downarrow} + \epsilon_R n_R + \gamma c^{\dagger}_{\downarrow} c_R + \gamma * c_{\downarrow} c^{\dagger}_R + J n_{\downarrow} n_R + U n_{\uparrow} n_{\downarrow}, \tag{9}$$

where we have redefined $\epsilon_{\uparrow} \equiv \epsilon_{L\uparrow}$, $\epsilon_{\downarrow} \equiv \epsilon_{L\downarrow}$, and $\epsilon_R \equiv \epsilon_{R\downarrow}$ for simplicity, now that the ambiguity between the spin and the L/R QD has been lifted. This approximation therefore leaves only one transport channel, which justifies the previously stated independence of γ on the spin.

3. Bosonic bath

The previous Hamiltonian does not feature a direct tunnel interaction between the two leads: any current flow can only result from quantum fluctuations of the on-site Coulomb interaction, triggering multiple electron processes. This connection is absent because the model does not take into account any spin-flip mechanism that would allow the jump of electrons between the lower spin ↑ level and the higher spin ↓ level on the left QD. The idea is now to optionally consider an interaction that would facilitate this spin flip, thereby allowing current to flow more easily through the dots. Intuition tells us that bosons may be good candidates for such a catalysis. Indeed, photons, phonons, vibrons, or magnons may bring sufficient energy to flip a spin. This could be possible at room temperature with phonons since the energy difference between the two spin energy levels may be of the order of $\delta \equiv \epsilon_{\downarrow} - \epsilon_{\uparrow} \approx$ 1–10 meV $\approx 10^2$ K [19,20].

Let us then add two terms to the Hamiltonian: the Hamiltonian of the bosonic bath

$$H_B = \sum_q \omega_q a_q^\dagger a_q, \tag{10}$$

where ω_q is the energy of the mode q and $a_q^\dagger$ and a_q are the bosonic laddering operators, and the Hamiltonian of coupling of the system to this bosonic bath

$$H_{SB} = \sum_q \lambda_q c_\uparrow^\dagger c_\downarrow (a_q + a_q^\dagger) + \text{H.c.}, \tag{11}$$

where λ_q represent the spin-boson couplings. We expect the distribution λ to be sharply peaked as only specific modes of the boson field will have the required energy to flip a spin. In the analytical part of this chapter, we will first discard the effect of this bath, which we will eventually turn on in the simulations.

B. Master equation

In Sec. 1 of the Supplemental Material [36], we use the Born approximation in the weak-coupling regime to establish the master equation describing the evolution of this open quantum system:

$$\begin{aligned}\frac{\mathrm{d}\rho}{\mathrm{d}t} =& -i[H_S, \rho] + \mathcal{T}_L^- \mathcal{D}[c_\uparrow^\dagger](\rho) + \mathcal{T}_L^+ \mathcal{D}[c_\uparrow](\rho) \\ &+ \mathcal{T}_R^- \mathcal{D}[c_R^\dagger](\rho) + \mathcal{T}_R^+ \mathcal{D}[c_R](\rho) \\ &+ \Lambda^- \mathcal{D}[c_\downarrow^\dagger c_\uparrow](\rho) + \Lambda^+ \mathcal{D}[c_\uparrow^\dagger c_\downarrow](\rho),\end{aligned} \tag{12}$$

where $\rho = \mathrm{Tr}_E\, \rho_{SE}$ is the QD system's reduced part of the full density matrix ρ_{SE} with respect to the environment degrees of freedom, $\mathcal{T}_L^-$ and $\mathcal{T}_R^-$ represent the electron hopping intensity between the QD and the left/right lead, respectively, while $\mathcal{T}_L^+$ and $\mathcal{T}_R^+$ are the hole counterparts, and with the superoperator $\mathcal{D}[c](\rho) \equiv c\rho c^\dagger - \frac{1}{2}\{c^\dagger c, \rho\}$. The last two terms represent the coupling to the bosonic bath that will be turned on later in Sec. III D: Λ^+ and Λ^- code for the pump and relaxation of the bosons, respectively. In what immediately follows, no explicit spin-flip mechanism is present. In the Supplemental Material [36], we give expressions for these coupling constants to the baths as a function of the filling of the energy levels of the baths and the couplings γ_k, γ_p, and λ_q. The magnitude of these coefficients thus depends on the thermodynamical parameters of the baths: temperature, chemical potential, etc. In the following, we will study the influence of these couplings on the engine and show that energy can be generated even when the baths are at thermodynamical equilibrium. We will also show that the power output can be greatly enhanced when a minimal nonequilibrium resource is considered.

C. Engine cycle

1. Phenomenological description and motivation

The theory of quantum mechanics involves two very distinct processes. A system first evolves through a continuous, linear, reversible, deterministic process described by the Schrödinger equation, and then is projected onto a definite state through the discrete, nonlinear, irreversible, and stochastic process of quantum measurements. Our QD system is subject to probing of its quantum state by the environment: its evolution first follows the master equation described above, followed by a projection due to the measurement. This very natural assumption is backed by several physical arguments.

Thermal, quantum, and shot noise in these magnetic junctions under quasiequilibrium conditions has been a matter of study [41–43] and suggests that quantum measurements could be linked to discrete charge fluctuations in the vicinity of the QD system. Further evidence showing nonlinear chaotic oscillations [44,45] in these devices along with rectification and feedback properties [46–48] also support the possibility of self-sustained oscillations in similar resonant tunneling quantum well structures, which could trigger these measurements.

In this context, a key element of our quantum spintronic engine is the ferromagnetic metal/molecule interface. This so-called "spinterface" exhibits a low density of spatiospectrally confined states with high spin polarization (89% [20]) at the Fermi level [19,20,38,39]. The proposal that a Maxwell demon can operate electronically at the molecular level [49], along with recent thermodynamic theory on quantum measurements [50–52], indicates that the spinterface could [20] act as an autonomous quantum measurement apparatus by performing frequent projective measurements on the nearby QD's spin state, thereby collapsing the WS's quantum state [53–55]. The ability of the ferromagnetic electrode to maintain a constant spin polarization, allowing it to behave as an entropy sink [20], also supports the possibility of these measurements. Indeed, information erasure would require a much lower entropy cost than the Landauer bound by involving the transfer of spin angular momentum into a large spin reservoir, rather than energy [56–58].

Following related studies that all postulate an external nonthermal quantum resource [17,18,27,28,31], and in line with the current conception of quantum mechanics that treat the measurement as a black box, we thus assume that the spinterface can perform these quantum measurements without an energy cost. Hence, we suppose that our device is endowed with a built-in autonomous quantum clock that frequently interacts with the system. In this article, we refrain from further describing the precise mechanisms that fuel this natural quantum clock, which we shall justify in detail in a future study.

Using our Hamiltonian, we consider a two-phased engine cycle (see Fig. 2). The first "thermalizing" stroke places the QDs into equilibrium with the electrode baths. The relaxation of the QD systems during this time-dependent evolution transfers energy from the system to the baths, some of which is harvested to produce useful electrical work. Then, once the system reaches its steady state, in which the two spin QDs are quantum correlated, the "measurement" stroke on a single QD splits the WS into two separated subsystems, thereby destroying coherence. As we shall show, this projective partial unselective measurement acting on a superposed mixed state with indefinite energy is mathematically described by a quantum channel that leads to a projected system with a higher average energy than the previous steady state. The measurement is thus generating quantum fluctuations by projecting the system from a global low-energy ground state to a local high-energy ground state. The energy difference that results from this back-action [5,17,28] of the measurement is then

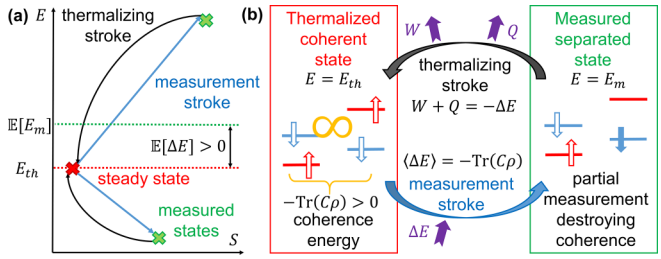

FIG. 2. Illustration of the engine cycle. (a) Energy-entropy illustration of the engine cycle. The unselective measurement stroke (straight blue arrows) instantly projects the thermalized steady state (red) onto several possible separated states (green) with higher entropy and potentially higher energy. The thermalizing strokes (curved black arrows) reset the system to the steady state while allowing for work extraction on average. (b) Illustration of the population of the energy levels during the two phases of the cycle. In the thermalized state, coherence energy is stored in the system; then the measurement stroke projects the right QD, destroying the superposition. The excessive energy of this localized ground state is then dissipated into the baths during the thermalizing stroke which restores coherence. In a solid-state implementation [19,20], these strokes reflect the inherent electronic interactions between a pair of exchange-coupled paramagnetic atoms, and with fully spin-polarized leads such as the ferromagnet/molecule interface [38].

dissipated into the baths during the next "thermalizing" stroke. We shall show that it can be used to produce electrical work.

2. *Analysis of the cycle*

Let us initialize our engine at $t_0 = 0$ in a state $\rho(0)$. After completing the first thermalization process, the electrode performs a partial projective measurement of the entangled QDs at time $t_1 \equiv \tau$, which represents the duration of one cycle. This measurement projects the system from the steady state $\rho(\tau^-) \equiv \overline{\rho}$, which may be only partially thermalized, to a projected state $\rho(\tau^+)$ that depends on the measurement outcome. Assuming that the right electrode operates frequent unselective measurements of the occupation of the right QD at times $t = t_n \equiv n\tau$, the associated observable is simply n_R. The measurement yields either the presence ($n_R = 1$) or the absence ($n_R = 0$) of one electron on the right QD. The two possible projectors on the respective eigenspaces are $\Pi_0 = 1 - n_R$ and $\Pi_1 = n_R$, leading to the projected state:

$$\rho(\tau^+) = \Pi_0 \overline{\rho} \Pi_0 + \Pi_1 \overline{\rho} \Pi_1 = \overline{\rho} + 2\mathcal{D}[n_R](\overline{\rho}). \tag{13}$$

Upon choosing the basis,

$$|0\rangle \equiv |00\rangle,\ |1\rangle \equiv |0\downarrow\rangle,\ |2\rangle \equiv |\uparrow 0\rangle,\ |3\rangle \equiv |\uparrow\downarrow\rangle,$$
$$|4\rangle \equiv |\downarrow 0\rangle,\ |5\rangle \equiv |\downarrow\downarrow\rangle,\ |6\rangle \equiv |20\rangle,\ |7\rangle \equiv |2\downarrow\rangle, \tag{14}$$

the density matrix ρ at all times can be cast under the form (see Sec. 3 of the Supplemental Material [36])

$$\sum_{i=0}^{7} \rho_{ii}|i\rangle\langle i| + \rho_{14}|1\rangle\langle 4| + \rho_{41}|4\rangle\langle 1| + \rho_{36}|3\rangle\langle 6| + \rho_{63}|6\rangle\langle 3|.$$

Note that the off-diagonal terms do not contribute to the projected state because they encode the tunneling of one electron from one site to the next, leaving either the initial state or the final state with no electron on the right side. Hence we calculate $\rho(\tau^+) = \sum_{i=0}^{7} \overline{\rho_{ii}}|i\rangle\langle i|$ so that $\rho(\tau^+)$ is the diagonal part of $\overline{\rho}$, while $-2\mathcal{D}[n_R](\overline{\rho})$ is the off-diagonal part.

The average energy of the system changes by an amount $\Delta E_1 \equiv \Delta E$,

$$\Delta E = \mathrm{Tr}[H_S \rho(\tau^+)] - \mathrm{Tr}[H_S \rho(\tau^-)], \tag{15}$$

which in turn represents the energy of the off-diagonal part,

$$\Delta E = -2\mathrm{Re}[\gamma(\overline{\rho}_{14} + \overline{\rho}_{36})] = -\langle C(\tau^-)\rangle = -\mathrm{Tr}[C\overline{\rho}]. \tag{16}$$

Here $C \equiv \gamma c_\downarrow^\dagger c_R + \gamma^* c_R^\dagger c_\downarrow$ is the interdot tunnel operator, which contains the coherence of the system. Thus, the measurement induces a back-action on the system by destroying the correlations, leading to an energy change ΔE compared to the thermalized state.

The energy increment gained after the nth cycle is $\Delta E_n \equiv -\mathrm{Tr}[C\rho(n\tau^-)]$. This shows that at time $t = n\tau^+$, if the system thermalizes completely to a unique steady state $\overline{\rho}$, then the system has received a total average energy $\sum_{k=1}^{n} \Delta E_k = n\Delta E = -n\mathrm{Tr}[C\overline{\rho}]$ from quantum measurements. Therefore, if $\Delta E > 0$, then the measurement on average energizes the system, and a fraction of that energy upon deexciting to the thermalized state can be harvested in the form of electron transport.

We tested other measurement scenarios (see Sec. 3 in the Supplemental Material [36]). We find that the engine operation/output is unchanged when measuring an observable that acts on only one QD [e.g., when the occupation of the left QD, or the charge (or spin) of the right QD, is measured]. Measuring an observable that operates on both QDs, such as the total charge, does not yield this energy increment: the thermalized and measured states have the same average energy. Work extraction from these cycles is possible only when the measurement separates the two QDs. If the quantum measurements are selective, then the energy increment relation holds by linearity while entropic considerations differ.

D. Thermodynamic quantities

The previous analysis of the cycle describes an engine that harvests the "quantum heat" ΔE. It is provided by the measurement, which acts like a hot heat bath that energizes the system. The systems then relaxes and dissipates its energy into the electrode baths, a fraction of which can be collected as a form of an electrical current to produce work. Let us then study briefly the thermodynamics of the cycle by applying the laws of thermodynamics during the thermalization stroke to evaluate the finality of the energy input ΔE provided by the measurement.

1. *Free energy*

The previous derivations allow us to define the maximum extractable work during the thermalization process. This quantity W_{th} is defined by the difference between the average free energy of the initial state at the beginning of a cycle at time $n\tau^+$ and the free energy of the final state at the end of the thermalizing stroke at time $(n+1)\tau^-$. So we obtain directly

$$W_{th} = -\Delta E + T\Delta S, \tag{17}$$

where ΔS is the difference in Von Neumann entropy between the states at times $n\tau^+$ and $(n+1)\tau^-$ (see Sec. 3 of the Supplemental Material [36] for precise estimations of this quantity for different measurement protocols). We can thus expect to extract energy at finite temperature whenever $W_{th} < 0$. It leads to a critical temperature $T_c \equiv \Delta E/\Delta S$ above which this engine cannot possibly work.

2. Efficiency

We may define the engine efficiency η as the ratio of the electronic work W_{el} obtained during the thermalization process to the total average energy provided by the quantum measurement:

$$\eta \equiv \frac{W_{el}}{\Delta E}. \tag{18}$$

By definition, this quantity is less than unity. Indeed, according to the first law of thermodynamics, which should hold during the time-dependent evolution of the thermalizing stroke according to Kumar and Stafford [59], we may write

$$-\Delta E = W_{el} + Q \tag{19}$$

with $-\Delta E \leqslant W_{th} \leqslant W_{el} \leqslant 0$ as we expect $Q \leqslant 0$ (see Fig. 2). This means that, if the measurement is energizing the system, heat should be dissipated to the reservoirs as the system thermalizes with the environment (a negative Q, with the same sign as W_{el}, means that the heat has been transferred from the system to the environment). Using this inequality, we should therefore have

$$\eta \leqslant -\frac{W_{th}}{\Delta E} \leqslant 1 - \frac{T}{T_c}, \tag{20}$$

so, as expected, the engine efficiency is still bounded by a form of the Carnot efficiency. As a final remark on this quantity, we should state that it does not have a very practical importance in the design of the engine as it can have in classical or other semiclassical quantum engines. Indeed, as our engine relies on the energy provided by autonomous quantum measurements performed by the environment, the fuel we are harvesting is present in infinite quantity in the self-sustained bath we are exploiting. Therefore, even a poor efficiency can be of interest given the limitless, constantly refueling amount of energy we are trying to harvest. We note that our formalism does not take into account the thermodynamic cost of information erasure as the spinterface electronically interacts with the ferromagnetic electrode acting as an entropy sink [20]. We suppose here that the overall energy balance will be favorable, and will address the thermodynamic cost of interfacial spin accumulation [60] in a future paper.

3. Power output

The power P follows instantly from the previous section. It is defined as

$$P \equiv -\frac{W_{el}}{\tau} \leqslant -\frac{W_{th}}{\tau} \leqslant \frac{\Delta E}{\tau} \equiv P_{\max}. \tag{21}$$

It is inversely proportional to the duration of a cycle. This means that devices with fast measurement frequencies can maximize this quantity. In the end, since only a fraction of the energy provided by the measurement stroke is recoverable as an electrical current, $P_{\max} = \frac{\Delta E}{\tau}$ provides at this point an upper bound of the electrical power generated by the device and thus represents a good estimation. In this article we shall not try to study the time-dependent dynamics of the thermalizing stroke to give a quantitative estimation of this fraction. We instead focus on ΔE, keeping in mind that the real engine might only deliver a portion of this energy at each cycle.

E. Perturbative solution

1. Density matrix in the perturbative regime

To gain numerical insights, we first derive the density matrix $\rho \equiv \rho_{ss}$ such as $\frac{d\rho}{dt} = 0$ so that ρ nullifies the right-hand side of Eq. (12). To obtain an approximate analytical solution, we use a perturbation approach on γ (see Sec. 2 in the Supplemental Material [36]), i.e., assume that other interaction energies dominate [20] the hybridization between the QDs. The solution is given by an affine space, parametrized by the initial population $\mu = \langle n_\downarrow(0)\rangle$ of the spin $\downarrow$ energy level on the left QD. We obtain the full density matrix ρ^μ after thermalization:

$$\begin{aligned}
\rho_{00} &= \frac{1-\mu}{\mu}\rho_{44} = \alpha(1-\mu)\mathcal{T}_L^+\mathcal{T}_R^+,\\
\rho_{11} &= \frac{1-\mu}{\mu}\rho_{55} = \alpha(1-\mu)\mathcal{T}_L^+\mathcal{T}_R^-,\\
\rho_{22} &= \frac{1-\mu}{\mu}\rho_{66} = \alpha(1-\mu)\mathcal{T}_L^-\mathcal{T}_R^+,\\
\rho_{33} &= \frac{1-\mu}{\mu}\rho_{77} = \alpha(1-\mu)\mathcal{T}_L^-\mathcal{T}_R^-,\\
\rho_{41} &= \rho_{14}^*\\
&= \frac{i\gamma\alpha\beta^\mu\mathcal{T}_L^+}{\det B^*}\left(\frac{2\mathcal{T}_L^+ + 2\mathcal{T}_L^- + \mathcal{T}_R^- + \mathcal{T}_R^+}{2} + i(\Delta + U)\right),\\
\rho_{63} &= \rho_{36}^*\\
&= \frac{i\gamma\alpha\beta^\mu\mathcal{T}_L^-}{\det B^*}\left(\frac{2\mathcal{T}_L^+ + 2\mathcal{T}_L^- + \mathcal{T}_R^- + \mathcal{T}_R^+}{2} + i\Delta\right),
\end{aligned}$$

where $\beta^\mu \equiv \mu\mathcal{T}_R^+ - (1-\mu)\mathcal{T}_R^-$, $1/\alpha \equiv (\mathcal{T}_L^+ + \mathcal{T}_L^-)(\mathcal{T}_R^+ + \mathcal{T}_R^-)$, $\Delta \equiv \epsilon_\downarrow - \epsilon_R$, B is referenced in Sec. 2 of the Supplemental Material [36], and the other terms are null.

To study the thermalized state of the next cycle, we consider the particle number with spin $\downarrow$ in the left QD. Since the projected state is diagonal, we directly obtain

$$\mathrm{Tr}[n_\downarrow\rho(\tau^+)] = \rho_{44} + \rho_{55} + \rho_{66} + \rho_{77} = \mu. \tag{22}$$

So, for both measurement outcomes, the spin $\downarrow$ occupation number remains unchanged after both the thermalizing and measurement strokes. Therefore, the second cycle starts again with $\langle n_\downarrow(\tau^+)\rangle = \mu$, and so it yields the same thermalized state just before the second measurement as in the previous cycle, such that $\rho(2\tau^-) = \rho(\tau^-) = \rho$ and thus an instant recursion yields the system state after each cycle n:

$$\rho(n\tau^+) = \rho(n\tau^-) + 2D[n_R](\rho) = \rho + 2D[n_R](\rho). \tag{23}$$

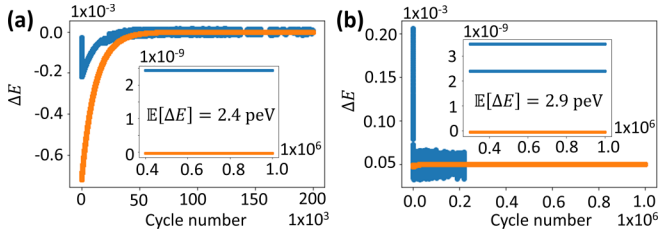

FIG. 3. Simulation results of ΔE for (a) $\rho_0 = |{\downarrow\downarrow}\rangle\langle{\downarrow\downarrow}|$ and (b) $\rho_0 = \frac{1}{2}|{\uparrow\downarrow}\rangle\langle{\uparrow\downarrow}| + \frac{1}{2}|{\downarrow\downarrow}\rangle\langle{\downarrow\downarrow}|$. The corrected perturbative results (orange) derived in Sec. 2 of the Supplemental Material [36], and the numerically calculated solution at 4 ps (blue) are shown. Here $\epsilon_\downarrow = 8$, $\epsilon_\uparrow = -3$, $\epsilon_R = 1$, $J = 8$, $U = 1000$, $\gamma = 0.1$, $\mathcal{T}_L^+ = \mathcal{T}_L^- = 0.1$, $\mathcal{T}_R^- = \mathcal{T}_R^+ = 0.01$; i.e., the two leads are both at infinite temperature (all units may be taken in meV and justification for their values may be found in Sec. 4 of the Supplemental Material [36]).

In this approximation, the total energy produced after the nth cycle will be $n\Delta E$ and the power output shall thus be $\frac{\Delta E}{\tau}$ where τ is the duration of a unit cycle.

2. *Energy in the perturbative regime*

We can express the energy $\Delta E = -2\mathrm{Re}[\gamma(\rho_{14} + \rho_{36})]$ associated with the measurement back-action as

$$\Delta E = \frac{\beta^\mu |\gamma|^2}{|\det B|^2} \frac{(s+r)^2}{sr}(s\Delta + mU), \tag{24}$$

with $s \equiv \mathcal{T}_L^+ + \mathcal{T}_L^-$, $m \equiv \mathcal{T}_L^-$, $r \equiv \frac{\mathcal{T}_R^+ + \mathcal{T}_R^-}{2}$, and

$$|\det B|^2 = r^2(r+s)^2 + [(s+2r)\Delta + (m+r)U]^2. \tag{25}$$

To study ΔE, we first assume (see Secs. 1 and 4 of the Supplemental Material [36]) that all the energies involved in the system $\mathcal{T}_L^+$, $\mathcal{T}_L^-$, $\mathcal{T}_R^+$, $\mathcal{T}_R^-$, Δ, and U are strictly positive. This immediately leads to $s, m, r > 0$ and then to ΔE having the same sign as β^μ. Therefore, the measurement energizes the two QDs whenever $\mu < \frac{\mathcal{T}_R^-}{\mathcal{T}_R^+ + \mathcal{T}_R^-} \equiv \mu^c$. Thus, at the critical value μ^c, the off-diagonal terms describing the first-order perturbation vanish, and the model cannot describe whether energy harvesting occurs.

III. SIMULATIONS

A. Simulating the engine's cycle

To evaluate these analytical results and confirm that the measurement reliably provides energy over many cycles, we simulated the engine operation. We show in Fig. 3 the results of measuring n_R across 10^6 cycles (see also Sec. 4 in the Supplemental Material [36]). Starting from the pure state $\rho_0 = |{\downarrow\downarrow}\rangle\langle{\downarrow\downarrow}|$, we first see in Fig. 3(a) that ΔE presents three trends: the first 10^5 cycles see an increase of ΔE towards 0, then a stochastic regime ensues where ΔE oscillates randomly around 0 until cycle number 4×10^5, before reaching a stable nonequilibrium steady state, where $\mathbb{E}[\Delta E] = 2.4$ peV. The drift originates from the partial thermalization, which gradually dilutes the information contained in the initial state ρ_0, resulting in a power output driven towards a steady-state attractor. Indeed, each new cycle introduces an additional mixing that can be understood as a statistical superposition of passive and active pure initial states which reduces the average energy increment of the next cycle.

To support this claim, in Fig. 3(b) we show that, starting from a mixed state $\rho_0 = \frac{1}{2}|{\uparrow\downarrow}\rangle\langle{\uparrow\downarrow}| + \frac{1}{2}|{\downarrow\downarrow}\rangle\langle{\downarrow\downarrow}|$, we find that ΔE converges more quickly towards a different power-generating limit cycle featuring two stable energy branches that result in $\mathbb{E}[\Delta E] = 2.9$ peV.

These simulations show that, during the transitional and stochastic regimes, the information on the initial condition is progressively lost through the nonunitary system evolution caused by thermalization, but it can never be entirely wiped out. Indeed, the engine acts as a chaotic nonergodic machine as we have shown that the system can get trapped in an active steady state when a certain priming is feeding favorable initial conditions.

In Sec. 4 of the Supplemental Material [36], we present additional data exploring different parameters, measurement protocols, as well as the case of selective measurements. These results show similar behaviors; i.e., all exhibit the ability to extract energy. The essential difference lies in the reading of the measurement. When using selective measurements, the situation changes qualitatively as the randomness of the measurement will frequently fail to energize the system and will instead place it in a lower energy state (see Fig. 2). This means that we cannot extract work during the thermalizing stroke for a large proportion of the cycles in which the measurement is taking energy from the system. It thus leads inevitably to a strongly chaotic behavior originating from the nonlinearity of the intrinsically stochastic measurement readout, which could then kill the efficiency of the device because of strong power fluctuations.

B. Partial thermalization

In Sec. 5 of the Supplemental Material [36], we test the speed of the thermalization process by comparing the calculated steady state of the master equation ρ with the density matrix σ calculated at time $t = 1$ meV$^{-1} \approx 4$ ps. This is considered to be a large upper bound of the duration of a cycle given the frequency bandwidth of the electronic interactions under consideration that should be linked to quantum measurements through charge transport fluctuations. As guidance, Chowrira *et al.* estimate a 140 THz electronic interaction frequency [20]. We consider ΔE, starting from different pure states and with different parameters taken randomly within an experimentally reasonable range [19,20].

The results presented show that the error made on the trace distance verifies $T(\rho, \sigma) < 0.9$ and leads to an error on the energy increment ΔE lower than 1% only for 1% of the test runs. This shows that, for a wide range of parameters, it is unreasonable to approximate the state at the end of the thermalizing stroke as the steady-state solution.

Thus, in this general case, we can only hope to reach a partial thermalization, though it is beneficial to the power output of the device, as it forces the system to stay out of equilibrium and to remain active even when it is connected to passive thermal baths. Indeed, statistics (not shown) on the steady-state entanglement energy reveal that, at infinite time $|\langle C\rangle| \approx 10^{-9}$–$10^{-16}$ meV for standard parameter ranges and passive thermal couplings, while after $t = 1$

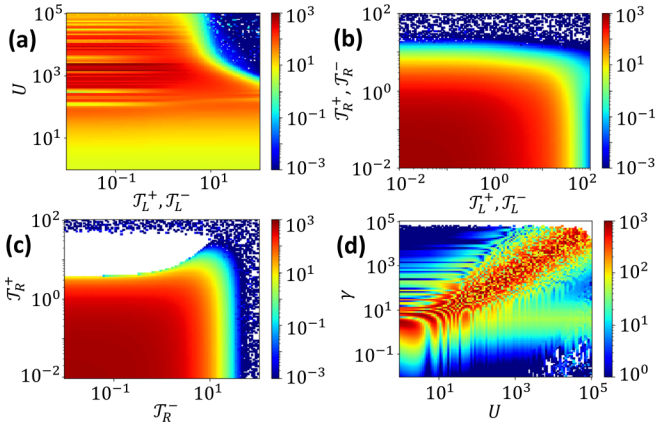

FIG. 4. Parameter pair dependence of the coherence energy $-\langle C\rangle$, calculated at 4 ps starting from the pure state $\rho_0 = |\uparrow\downarrow\rangle\langle\uparrow\downarrow|$, with $\epsilon_\downarrow = 8$, $\epsilon_\uparrow = -3$, $\epsilon_R = 1$, $J = 8$, $U = 1000$, $\gamma = 1000$, $\mathcal{T}_L^+ = \mathcal{T}_L^- = \mathcal{T}_R^+ = \mathcal{T}_R^- = 0.1$. (a) $\mathcal{T}_L^+ = \mathcal{T}_L^-$ versus U, (b) $\mathcal{T}_L^+ = \mathcal{T}_L^-$ versus $\mathcal{T}_R^+ = \mathcal{T}_R^-$, (c) $\mathcal{T}_R^-$ versus $\mathcal{T}_R^+$, (d) U versus γ.

meV$^{-1} \approx 4$ ps, we can reach up to $|\langle C\rangle| \approx 10^3$ meV and obtain an energy-generating limit cycle while in the same equilibrium parameter configuration for special initial conditions. This suggests a higher energy increment. Indeed, the average energy increment per cycle is still given by $\Delta E = -\langle C\rangle$ in this general case, so that the previous energetic description of the cycle remains valid here. A proof of this assertion is given in Sec. 3 of the Supplemental Material [36], along with a numerical justification based on measurement statistics.

C. Maximizing the coherence energy

To study how the parameters that impact the partially thermalized state ρ affect the coherence energy $-\langle C\rangle$, we show in Fig. 4 several color plots of $-\langle C\rangle$ calculated after the thermalizing stroke starting from the pure state $\rho_0 = |\uparrow\downarrow\rangle\langle\uparrow\downarrow|$ as a function of the most relevant different pairs of parameters (see Sec. 6 of the Supplemental Material [36] for other plots), keeping other parameters fixed, and with $\gamma \sim U \gg \epsilon \gg \mathcal{T}$.

In Fig. 4(a), we notice that $-\langle C\rangle$ is maximized when $U \approx 10^3$–10^4 and $\mathcal{T}_L^+ = \mathcal{T}_L^- < 1$. Indeed, a higher U could lead to a bigger coherence energy that is related to the charging energy of a QD, while a lower $\mathcal{T}_L$ favors the tunneling between the QDs over the tunneling from/to the electrodes. In Fig. 4(b), we observe that the asymmetry between $\mathcal{T}_L$ and $\mathcal{T}_R$ is quite irrelevant for this set of parameters for low $\mathcal{T}_R$: the engine generates power and energy harvesting may be possible.

Above a phase transition around $\mathcal{T}_R \approx 10$ [see also Fig. 4(d)], a chaotic phase ensues, coherence energy almost vanishes, and its sign strongly depends on small parameter fluctuations: we cannot extract energy in this configuration [61]. Intuitively, this chaotic phase results from a dominating interaction with the right electrode that completely overcomes the tunneling interaction between the QDs, thereby nullifying the potential entanglement energy between the two sites.

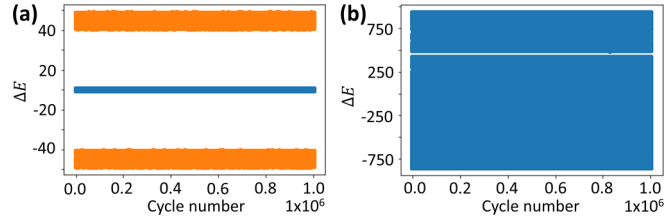

FIG. 5. Simulation results of ΔE for 10^6 cycles when measuring the charge Q of the left QD using (a) unselective and (b) selective measurements. The numerical calculation (orange) and the perturbative solution (blue) are shown. $\epsilon_\downarrow = 8$, $\epsilon_\uparrow = -3$, $\epsilon_R = 1$, $J = 8$, $U = 1000$, $\gamma = 1000$, $\mathcal{T}_L^+ = \mathcal{T}_R^+ = \mathcal{T}_L^- = \mathcal{T}_R^- = 0.1$ (all units may be taken in meV), and with the initial condition $\rho_0 = |\uparrow\downarrow\rangle\langle\uparrow\downarrow|$.

In Fig. 4(c), we examine the electron/hole asymmetry on the right electrode. The data reveal a third, dissipative phase with no energy extraction with $-\langle C\rangle < 0$ (in white).

Finally, in Fig. 4(d), the U/γ dependence reveals two branches that maximize coherence energy: one for $\gamma \approx 1$ that weakly depends on U, and a second for $\gamma \approx U$. This may help tune experimental device parameters to maximize energy harvesting as these data show an advantage in strong Coulombic repulsion U along with a strong interdot coupling g, indicating that the two sites should be close and have a large electronic affinity.

Although maximizing ΔE starting from a particular initial state is a first step towards finding the maximum power output, it is not straightforwardly linked to the power output since it corresponds to an average over many cycles with different initial states.

D. Power fluctuations

Using the data of Fig. 4 along with Sec. 6 in the Supplemental Material [36], we infer a regime wherein the entanglement energy is highest with $\mathcal{T} \ll \epsilon \ll \gamma \approx U \approx 1000\epsilon$. To confirm the high power output $P = \frac{\mathbb{E}[\Delta E]}{\tau}$ within this parameter space, we simulated 10^6 engine cycles (see plots in Fig. 5). Strikingly, we observe strong fluctuations of ΔE that ultimately kill the temporal average of the energy increment. This shows that maximizing $-\langle C\rangle$ also yields a strong dependence of the tunneling energy after partial thermalization on the initial conditions. This increases the fluctuations and negatively impacts P: maximizing P requires balancing energy and fluctuations. Indeed, from the Heisenberg uncertainty relations, when selectively measuring n_R, we may write

$$\Delta C \Delta n_R \geqslant \frac{1}{2}|\langle [C, n_R]\rangle| = \frac{1}{2}|\langle [H_S, n_R]\rangle| \approx \frac{1}{2}\left|\frac{\mathrm{d}\langle n_R\rangle}{\mathrm{d}t}\right|. \quad (26)$$

Here, at the end of each cycle, $\Delta n_R \lesssim 1$ is known and fixed by the statistical outcomes of the measurements and should be of order unity since the measurement alternatively projects the system into a state with $n_R = 0$ or $n_R = 1$. Moreover, the right-hand side describes the n_R oscillation rate, which is strongly driven by the energy scale of the coherence energy $|\langle C\rangle|$. Thus, Eq. (26) justifies that $\Delta C \gtrsim |\langle C\rangle|$.

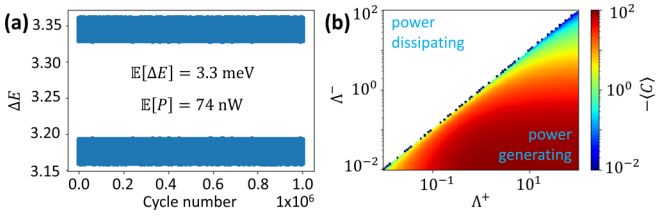

FIG. 6. (a) Simulation results of ΔE for 10^6 cycles powered by a nonthermal bosonic bath when measuring the population n_R in the case of two identical electrodes at thermal equilibrium with infinite temperature. Parameters are $\epsilon_\downarrow = 8$, $\epsilon_\uparrow = -3$, $\epsilon_R = 1$, $J = 8$, $U = 1000$, $\gamma = 1000$, $\mathcal{T}_L^+ = \mathcal{T}_R^+ = \mathcal{T}_L^- = \mathcal{T}_R^- = 0.1$, and $\Lambda^+ = 2\Lambda^- = 0.01$. (b) Color plot of $-\langle C\rangle$ calculated at 4 fs as a function of the bosonic coupling parameters Λ^+ and Λ^-, starting from the pure state $\rho_0 = |\uparrow\downarrow\rangle\langle\uparrow\downarrow|$. All other parameters are the same as in (a).

A second Heisenberg inequality can be written regarding the initial condition decisive observable $n_\downarrow$, which shows that the fluctuations of T are also related to the momentum dispersion of the initial conditions $\dot{\mu}$, which is mainly impacted by the partial thermalization. For some parameters, the characteristic time of the system is such that it keeps the information about its initial state longer in memory, thus resulting in stronger fluctuations that can also be observed for the unselective case [see Fig. 5(a)].

E. Bosonic catalysis

1. Powering the engine with a bosonic pump

Our work thus showcases how to harvest energy as an electrical current between two leads across quantum dots despite no direct electronic connection, i.e., how to generate continuous power from quantum fluctuations generated by the measurement back-action. The predicted output power is much lower than that measured [19,20], which suggests the experimental presence of an additional quantum resource. Since our QDs are embedded in an atomic matrix, we examine the impact of bosons, such as spintronic magnons, lattice phonons, or vibrons on the QD complex, through an additional interaction with a bosonic bath that can flip the spin of the left dot [see Eq. (12)]. We then repeated the experiments presented in Figs. 3 and 4.

As expected, Fig. 6(b) shows that the device remains passive whenever the system interacts with a thermal bath in which $\Lambda^- > \Lambda^+$ for the same equilibrium parameters as above. Nonetheless, the simulation presented in Fig. 6(a) shows that the energy increment ΔE can reach up to $\Delta E \approx 10$ meV for a weak asymmetric coupling $\Lambda^+ = 2\Lambda^- = 0.01$ (negative temperature), leading to a power output $P \approx 100$ nW when choosing a cycle duration triggered by the electronic frequency of $\tau^{-1} = 140$ THz in line with a prior report [20]. This bosonic pump greatly decreases the thermalization time: the information on the initialization of each cycle is almost completely removed, and relative power fluctuations are much lower compared to having only vacuum fluctuations.

It is possible to engineer this autonomous nonthermal bosonic interaction using a finite bath (the complex vibrons) coupled to a larger infinite thermal bath (the lattice phonons). This would generate the nonunitary coupling Hamiltonian necessary to build such asymmetric coefficients through squeezing [7,24,26,32], broken symmetries [62], non-Hermitian skin effect [63,64], or nonlinear processes [65]. We leave details of this nonthermal bosonic bath to future studies.

2. Powering the engine with a spin bias

Although a nonthermal bosonic bath might be present in our spintronic engine, without further evidence, supposing the influence of such a drive is not satisfactory. Let us then look for another nonthermal resource that can power the device, and suppose that the bosonic bath is thermal, meaning that $\Lambda^- > \Lambda^+$.

Following the formalism of thermodynamics with conserved quantities [66], thanks to the fixed magnetization of the electrodes, we can consider the spinterfaces as mesoscopic spin reservoirs for which spin polarization is a conserved quantity. Let us then focus on the left electrode, considered as the reference. Its free energy then reads

$$F_L = \langle H_L\rangle - \mu_L\langle N_L\rangle - m_L\langle P_L\rangle - T_L S_L, \tag{27}$$

where H_L has been defined in Eq. (5), $N_L = \sum_{k,\sigma} n_{k,\sigma}$ is the total number operator on the left, $P_L = \sum_k n_{k,\uparrow} - n_{k,\downarrow}$ is the spin polarization operator, $S_R = \mathrm{Tr}(\rho_L \ln \rho_L)$ is the Von Neumann entropy, and μ_L, m_L, and T_L are the conjugated generalized charges such that μ_L is the usual electrochemical potential, T_L is the temperature, and m_L is a spin potential.

The generalized Gibbs state τ_L corresponding to this spin reservoir thus reads

$$\tau_L = \mathcal{Z}_L^{-1} e^{-\beta_L(H_L - \mu_L N_L - m_L P_L)}, \tag{28}$$

where

$$\mathcal{Z}_L = \mathrm{Tr}(e^{-\beta_L(H_L - \mu_L N_L - m_L P_L)}). \tag{29}$$

Using the commutation relations of the individual number operators, we obtain

$$\mathcal{Z}_L = \prod_{k,\sigma}[1 + e^{-\beta_L(\epsilon_{k,\sigma} - \mu_L - \sigma m_L)}] \tag{30}$$

and therefore

$$\langle n_{k,\sigma}\rangle = \mathrm{Tr}\, n_{k,\sigma}\tau = \frac{1}{1 + e^{\beta_L(\epsilon_{k,\sigma} - \mu_L - \sigma m_L)}}. \tag{31}$$

The same expression can be obtained for the right electrode with its respective parameters β_R, μ_R, and m_R. In the case where the electrodes' filling is well described by a strong magnetization, we can discard the energy term and feed

$$\langle n_{k,\sigma}\rangle = \frac{1}{1 + e^{-\beta_L(\mu_L + m_L)}},$$
$$\langle n_{p,\sigma}\rangle = \frac{1}{1 + e^{-\beta_R(\mu_R - m_R)}} \tag{32}$$

into the expressions for $\mathcal{T}_L^+$, $\mathcal{T}_L^-$, $\mathcal{T}_R^+$, and $\mathcal{T}_R^-$ reported in Sec. 1 of the Supplemental Material [36] such as we can engineer $\mathcal{T}_L^- < \mathcal{T}_L^+$ and $\mathcal{T}_R^+ < \mathcal{T}_R^-$ for well chosen m_L and m_R by acting on their magnetization. This holds even if the two electrodes have the same temperature $\beta_L = \beta_R$ and chemical potential $\mu_L = \mu_R$. This calculation thus shows that the coupling coefficients to the bath can be tuned either by acting on electronic potential, or on its magnetization, such that a

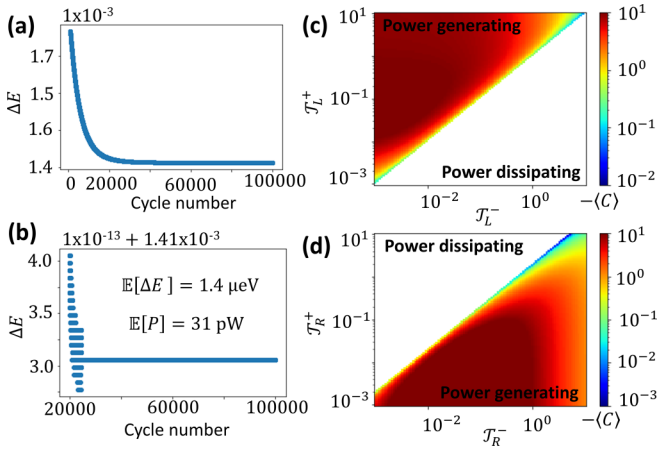

FIG. 7. Simulation of the engine with bosonic catalysis powered by a spin bias. (a) and (b) Simulation results of ΔE for 10^6 cycles powered by a spin bias bath when measuring the population n_R. Parameters are $\epsilon_\downarrow = 8$, $\epsilon_\uparrow = -3$, $\epsilon_R = 1$, $J = 8$, $U = 1000$, $\gamma = 1000$, $\mathcal{T}_L^+ = 0.2, \mathcal{T}_R^+ = \mathcal{T}_L^- = \mathcal{T}_R^- = 0.1$, $\Lambda^+ = 0.01$, and $\Lambda^- = 0.0101$. (c) Color plot of $-\langle C\rangle$ calculated for the steady state as a function of the bosonic coupling parameters $\mathcal{T}_L^-$ and $\mathcal{T}_L^+$, starting from the pure state $\rho_0 = |\uparrow\downarrow\rangle\langle\uparrow\downarrow|$. All other parameters are the same as in (a). (d) Color plot of $-\langle C\rangle$ as a function of $\mathcal{T}_R^-$ and $\mathcal{T}_R^+$ with the same set of parameters.

"spin bias" can yield the necessary asymmetry required for the device to run as an engine.

The spin bias, corresponding to a difference in the magnetic potential of the two electrodes, can be engineered by choosing electrodes featuring different intrinsic spin polarizations, or by imposing a magnetization difference between the two ferromagnets. This may be achieved by engineering noncollinear magnetizations using magnetic anisotropy, or simply by choosing electrode materials with different magnetization amplitudes. This thermodynamical resource should therefore persist naturally in our device for an indefinite time without requiring an external energy supply.

In Fig. 7(a) we show a test run for the engine, using a thermal bosonic bath with $\Lambda^- > \Lambda^+$, and with a regular asymmetry $\mathcal{T}_L^- < \mathcal{T}_L^+$ and $\mathcal{T}_R^+ = \mathcal{T}_R^-$. After about 10^5 cycles, the engine stabilizes in a generative steady state delivering an average of 1.4 μeV per cycle. This shows that a nonthermal bosonic pump is not necessary to run the engine with a high output power that can mimic the experiments: a favorable asymmetry of the coupling coefficients to the baths, which is finely tuned by a built-in spin bias originating from the magnetization of the electrodes, is sufficient to power the engine.

In Figs. 7(b) and 7(c), we study the dependence of the coherence energy $-\langle C\rangle$ obtained in the steady state of the master equation with respect to the pairs of parameters $\mathcal{T}_L^-, \mathcal{T}_L^+$ and $\mathcal{T}_R^+, \mathcal{T}_R^-$ for the same set of parameters as the test run and show that the device behaves as an engine whenever $\mathcal{T}_L^- < \mathcal{T}_L^+$ and $\mathcal{T}_R^+ < \mathcal{T}_R^-$, meaning that the left electrode should favor down-spin filling with $m_L > -\mu_L$ and the right electrode should favor up spins with $m_R < \mu_R$.

In Sec. 7 of the Supplemental Material [36], we provide more data about this bosonic catalysis, study the influence of the different parameters, and show that this power level can also be recovered if we replace the assumption of a negative temperature bosonic bath or a spin bias by another, standard nonequilibrium resource such as a potential or a temperature difference.

IV. CONCLUSION

We studied a quantum information engine built around autonomous solid-state spintronic interactions that can harvest the energy of quantum coherence and can explain recent experiments involving atomic spin qubits [19,20]. Our model considered a pair of correlated spin quantum dots that electronically interact with spin-selecting electrodes. We derived a master equation that describes a two-step engine: a thermalizing stroke that creates coherence between the two quantum dots and generates electron transport, then a quantum measurement stroke that extracts energy from their correlation. This changes their entropy by separating and projecting the system into a higher energy state on average. When quantum fluctuations induced by the measurement—understood as the difference between the ground energy states of a thermal system and a system with the measurement interactions turned on—constitute the only energy source, numerical simulations predict an appreciable finite power output in some cases. We reproduce experimentally measured power levels [20] by including a bosonic bath along with a nonthermal resource, such as the spin bias that is naturally present in our system due to the ferromagnetic electrodes. Our work thus explains recent [19,20] and perhaps also older [40,67] experiments, and showcases the ferromagnet/molecule interface (the spinterface [38,39]) with high spin polarization [20] as a quantum measurement apparatus. It also provides parametric insight into possible priming conditions to start the engine.

Our study sheds light on a quantum engine that relies on quantum measurements in order to extract energy from a system of coupled quantum dots, through the breaking of coherence energy. Using a perturbative approach, we found a regime of parameters for such a system that could lead to energy generation during a large number of cycles, and we confirmed this finding using numerical simulation. Then, we proceeded to find a good set of parameters that can maximize the power output by maximizing the coherence energy generated after each thermalization process, but we found that this gain in energy increment was compensated by increasing fluctuations due to partial thermalization, which ultimately negatively impacts the expected power output. A compromise between fluctuations and the maximum energy output should thus be found in order to maximize the power output but the present study was so far unable to find this optimum. Future work should be able to gain more insights on this point and prove rigorously the definite harvesting capabilities of the device after a long time using ergodic theory.

The present study only focused on the energetics of the device brought by the measurement process. Hence, we could only set a higher bound for the power output, corresponding to the energy we can hope to extract at zero temperature when no energy is lost thorough irreversible heat exchanges. In order to obtain a more realistic depiction of the thermodynamics of the system at finite temperature and electrochemical potentials,

more efforts need to be dedicated towards the study of the thermalization process. This issue will also be the subject of a future work, which will aim at applying the first law of thermodynamics during the time-dependent evolution of the system in order to clearly separate the electrical work we are interested in from the heat that is dissipated during the thermalizing stroke.

Finally, this article opens fruitful research into spintronic interaction dynamics between ferromagnets and paramagnetic centers [68], e.g., using scanning tunneling and ferromagnetic resonance techniques [69], to elucidate the thermodynamic role [56,58] of the spintronic quantum measurement apparatus [19,20].

ACKNOWLEDGMENTS

We thank C. Elouard, E. Lutz, J. Monsel, K. Singer, I. Khomchenko, and R. Whitney for stimulating discussions. We gratefully acknowledge Ph.D. funding for M.L. from Ecole Polytechnique. We acknowledge financial support from the ANR (Grant No. ANR-21-CE50-0039), the Contrat de Plan Etat-Region grants in 2006 and 2008, by "NanoTerahertz," a project co-funded by the ERDF 2014–2020 in Alsace (European Union fund), and by the Region Grand Est through its FRCR call, by the impact project LUE-N4S part of the French PIA project "Lorraine Université d'Excellence," Reference No. ANR-15IDEX-04-LUE, and by the FEDER-FSE "Lorraine et Massif Vosges 2014–2020," a European Union program. This "SpinDrive" work of the Interdisciplinary Thematic Institute QMat, as part of the ITI 2021–2028 program of the University of Strasbourg, CNRS, and Inserm, was supported by IdEx Unistra (Grant No. ANR 10 IDEX 0002), and by the SFRI STRAT'US project (Grant No. ANR 20 SFRI 0012) and EUR QMAT ANR-17-EURE-0024 under the framework of the French Investments for the Future Program. Funding through the French PEPR Spin (Grant No. ANR-22-EXSP-0007) is gratefully acknowledged.

[1] S. Vinjanampathy and J. Anders, Quantum thermodynamics, Contemp. Phys. **57**, 545 (2016).
[2] S. Rogers and A. N. Jordan, Postselection and quantum energetics, Phys. Rev. A **106**, 052214 (2022).
[3] S. Bhattacharjee and A. Dutta, Quantum thermal machines and batteries, Eur. Phys. J. B **94**, 239 (2021).
[4] K. Ptaszyński, Autonomous quantum Maxwell's demon based on two exchange-coupled quantum dots, Phys. Rev. E **97**, 012116 (2018).
[5] S. Seah, S. Nimmrichter, and V. Scarani, Maxwell's lesser demon: A quantum engine driven by pointer measurements, Phys. Rev. Lett. **124**, 100603 (2020).
[6] G. Piccitto, M. Campisi, and D. Rossini, The Ising critical quantum Otto engine, New J. Phys. **24**, 103023 (2022).
[7] G. Manzano, F. Galve, R. Zambrini, and J. M. R. Parrondo, Entropy production and thermodynamic power of the squeezed thermal reservoir, Phys. Rev. E **93**, 052120 (2016).
[8] O. A. D. Molitor and G. T. Landi, Stroboscopic two-stroke quantum heat engines, Phys. Rev. A **102**, 042217 (2020).
[9] B. Donvil, Thermodynamics of a periodically driven qubit, J. Stat. Mech.: Theory Exp. (2018) 043104.
[10] F. Zhao, F.-Q. Dou, and Q. Zhao, Quantum battery of interacting spins with environmental noise, Phys. Rev. A **103**, 033715 (2021).
[11] T. F. F. Santos and M. F. Santos, Efficiency of optically pumping a quantum battery and a two-stroke heat engine, Phys. Rev. A **106**, 052203 (2022).
[12] G. Francica, F. Binder, G. Guarnieri, M. Mitchison, J. Goold, and F. Plastina, Quantum coherence and ergotropy, Phys. Rev. Lett. **125**, 180603 (2020).
[13] Y.-H. Shi, H.-L. Shi, X.-H. Wang, M.-L. Hu, S.-Y. Liu, W.-L. Yang, and H. Fan, Quantum coherence in a quantum heat engine, J. Phys. A: Math. Theor. **53**, 085301 (2020).
[14] S. Aimet and H. Kwon, Engineering a heat engine purely driven by quantum coherence, Phys. Rev. A **107**, 012221 (2023).
[15] J. Monsel, M. Fellous-Asiani, B. Huard, and A. Auffèves, The energetic cost of work extraction, Phys. Rev. Lett. **124**, 130601 (2020).
[16] L. Buffoni, A. Solfanelli, P. Verrucchi, A. Cuccoli, and M. Campisi, Quantum measurement cooling, Phys. Rev. Lett. **122**, 070603 (2019).
[17] L. Bresque, P. A. Camati, S. Rogers, K. Murch, A. N. Jordan, and A. Auffèves, Two-qubit engine fueled by entanglement and local measurements, Phys. Rev. Lett. **126**, 120605 (2021).
[18] E. Jussiau, L. Bresque, A. Auffèves, K. W. Murch, and A. N. Jordan, Many-body quantum vacuum fluctuation engines, Phys. Rev. Res. **5**, 033122 (2023).
[19] K. Katcko, E. Urbain, B. Taudul, F. Schleicher, J. Arabski, E. Beaurepaire, B. Vileno, D. Spor, W. Weber, D. Lacour, S. Boukari, M. Hehn, M. Alouani, J. Fransson, and M. Bowen, Spin-driven electrical power generation at room temperature, Commun. Phys. **2**, 116 (2019).
[20] B. Chowrira, L. Kandpal, M. Lamblin, F. Ngassam, C. Kouakou, T. Zafar, D. Mertz, B. Vileno, C. Kieber, G. Versini, B. Gobaut, L. Joly, T. Ferté, E. Monteblanco, A. Bahouka, R. Bernard, S. Mohapatra, H. Prima Garcia, S. Elidrissi, M. Gavara *et al.*, Quantum advantage in a molecular spintronic engine that harvests thermal fluctuation energy, Adv. Mater. **34**, 2206688 (2022).
[21] J. Klatzow, J. N. Becker, P. M. Ledingham, C. Weinzetl, K. T. Kaczmarek, D. J. Saunders, J. Nunn, I. A. Walmsley, R. Uzdin, and E. Poem, Experimental demonstration of quantum effects in the operation of microscopic heat engines, Phys. Rev. Lett. **122**, 110601 (2019).
[22] W. Ji, Z. Chai, M. Wang, Y. Guo, X. Rong, F. Shi, C. Ren, Y. Wang, and J. Du, Spin quantum heat engine quantified by quantum steering, Phys. Rev. Lett. **128**, 090602 (2022).
[23] K. Micadei, J. P. S. Peterson, A. M. Souza, R. S. Sarthour, I. S. Oliveira, G. T. Landi, T. B. Batalhão, R. M. Serra, and E. Lutz,

Reversing the direction of heat flow using quantum correlations, Nat. Commun. **10**, 2456 (2019).
[24] W. Niedenzu, V. Mukherjee, A. Ghosh, A. G. Kofman, and G. Kurizki, Quantum engine efficiency bound beyond the second law of thermodynamics, Nat. Commun. **9**, 165 (2018).
[25] J. Roßnagel, O. Abah, F. Schmidt-Kaler, K. Singer, and E. Lutz, Nanoscale heat engine beyond the Carnot limit, Phys. Rev. Lett. **112**, 030602 (2014).
[26] J. Klaers, S. Faelt, A. Imamoglu, and E. Togan, Squeezed thermal reservoirs as a resource for a nanomechanical engine beyond the Carnot limit, Phys. Rev. X **7**, 031044 (2017).
[27] M. O. Scully, Extracting work from a single heat bath via vanishing quantum coherence, Science **299**, 862 (2003).
[28] J. Yi, P. Talkner, and Y. W. Kim, Single-temperature quantum engine without feedback control, Phys. Rev. E **96**, 022108 (2017).
[29] C. Elouard and A. N. Jordan, Efficient quantum measurement engines, Phys. Rev. Lett. **120**, 260601 (2018).
[30] G. Francica, J. Goold, F. Plastina, and M. Paternostro, Daemonic ergotropy: Enhanced work extraction from quantum correlations, npj Quantum Inf. **3**, 12 (2017).
[31] C. Elouard, D. Herrera-Martí, B. Huard, and A. Auffèves, Extracting work from quantum measurement in Maxwell's demon engines, Phys. Rev. Lett. **118**, 260603 (2017).
[32] Y. Xiao, D. Liu, J. He, L. Zhuang, W.-M. Liu, L.-L. Yan, and J. Wang, Thermodynamics and fluctuations in finite-time quantum heat engines under reservoir squeezing, Phys. Rev. Res. **5**, 043185 (2023).
[33] J. Fransson and M. Råsander, Pauli spin blockade in weakly coupled double quantum dots, Phys. Rev. B **73**, 205333 (2006).
[34] I. Weymann and J. Barnaś, Transport through two-level quantum dots weakly coupled to ferromagnetic leads, J. Phys.: Condens. Matter **19**, 096208 (2007).
[35] J. Fransson, J. Ren, and J.-X. Zhu, Electrical and thermal control of magnetic exchange interactions, Phys. Rev. Lett. **113**, 257201 (2014).
[36] See Supplemental Material at http://link.aps.org/supplemental/10.1103/PhysRevB.109.165423 for the full derivation of the master equation; the perturbative solution; precision on energy and entropy for different measurement protocols; additional engine simulation results; sampling numerical experiments; details on the maximization of coherence energy and bosonic catalysis. It also contains Refs. [70–73].
[37] M. Bowen, A. Barthélémy, V. Bellini, M. Bibes, P. Seneor, E. Jacquet, J.-P. Contour, and P. H. Dederichs, Observation of Fowler–Nordheim hole tunneling across an electron tunnel junction due to total symmetry filtering, Phys. Rev. B **73**, 140408 (2006).
[38] F. Djeghloul, M. Gruber, E. Urbain, D. Xenioti, L. Joly, S. Boukari, J. Arabski, H. Bulou, F. Scheurer, F. Bertran, P. Le Fèvre, A. Taleb-Ibrahimi, W. Wulfhekel, G. Garreau, S. Hajjar-Garreau, P. Wetzel, M. Alouani, E. Beaurepaire, M. Bowen, and W. Weber, High spin polarization at ferromagnetic metal–organic interfaces: A generic property, J. Phys. Chem. Lett. **7**, 2310 (2016).
[39] S. Delprat, M. Galbiati, S. Tatay, B. Quinard, C. Barraud, F. Petroff, P. Seneor, and R. Mattana, Molecular spintronics: The role of spin-dependent hybridization, J. Phys. D: Appl. Phys. **51**, 473001 (2018).
[40] G.-X. Miao, J. Chang, B. A. Assaf, D. Heiman, and J. S. Moodera, Spin regulation in composite spin-filter barrier devices, Nat. Commun. **5**, 3682 (2014).
[41] S. Larocque, E. Pinsolle, C. Lupien, and B. Reulet, Shot noise of a temperature-biased tunnel junction, Phys. Rev. Lett. **125**, 106801 (2020).
[42] J. P. Cascales, L. Martin, A. Dulluard, M. Hehn, C. Tiusan, T. Szczepanski, V. Dugaev, J. Barnas, and F. G. Aliev, Shot noise in epitaxial double-barrier magnetic tunnel junctions, IEEE Trans. Magn. **49**, 4347 (2013).
[43] H.-Q. Guo, W.-Y. Tang, L. Liu, J. Wei, D.-L. Li, J.-F. Feng, and X.-F. Han, Low frequency noise in asymmetric double barrier magnetic tunnel junctions with a top thin MgO layer, Chin. Phys. B **24**, 078504 (2015).
[44] C. Ertler and J. Fabian, Self-sustained magnetoelectric oscillations in magnetic resonant tunneling structures, Phys. Rev. Lett. **101**, 077202 (2008).
[45] P. Zhao, D. L. Woolard, and H. L. Cui, Multisubband theory for the origination of intrinsic oscillations within double-barrier quantum well systems, Phys. Rev. B **67**, 085312 (2003).
[46] R. Bo, Q. Xu, Y. Qian, J. Du, and Z. Zhang, Controllable spin diode based on a semiconductor quantum dot, Jpn. J. Appl. Phys. **61**, 060910 (2022).
[47] G. Jona-Lasinio, C. Presilla, and F. Capasso, Chaotic quantum phenomena without classical counterpart, Phys. Rev. Lett. **68**, 2269 (1992).
[48] J. Galan and E. Freire, Chaos in a mean field model of coupled quantum wells; bifurcations of periodic orbits in a symmetric Hamiltonian system, Rep. Math. Phys. **44**, 87 (1999).
[49] J. P. Bergfield, S. M. Story, R. C. Stafford, and C. A. Stafford, Probing Maxwell's demon with a nanoscale thermometer, ACS Nano **7**, 4429 (2013).
[50] G. Manzano, F. Plastina, and R. Zambrini, Optimal work extraction and thermodynamics of quantum measurements and correlations, Phys. Rev. Lett. **121**, 120602 (2018).
[51] N. Erez, G. Gordon, M. Nest, and G. Kurizki, Thermodynamic control by frequent quantum measurements, Nature (London) **452**, 724 (2008).
[52] N. Erez, Thermodynamics of projective quantum measurements, Phys. Scr. **T151**, 014028 (2012).
[53] G. Lindblad, Entropy, information and quantum measurements, Commun. Math. Phys. **33**, 305 (1973).
[54] K. Jacobs, Quantum measurement and the first law of thermodynamics: The energy cost of measurement is the work value of the acquired information, Phys. Rev. E **86**, 040106(R) (2012).
[55] M. Ban, State reduction, information and entropy in quantum measurement processes, J. Phys. A: Math. Gen. **32**, 1643 (1999).
[56] J. S. S. T. Wright, T. Gould, A. R. R. Carvalho, S. Bedkihal, and J. A. Vaccaro, Quantum heat engine operating between thermal and spin reservoirs, Phys. Rev. A **97**, 052104 (2018).
[57] E. Bormashenko, Entropy, information, and symmetry; ordered is symmetrical, II: System of spins in the magnetic field, Entropy **22**, 235 (2020).

[58] J. A. Vaccaro and S. M. Barnett, Information erasure without an energy cost, Proc. R. Soc. London A **467**, 1770 (2011).

[59] P. Kumar and C. A. Stafford, On the first law of thermodynamics in time-dependent open quantum systems, arXiv:2208.06544.

[60] T. Valet and A. Fert, Theory of the perpendicular magnetoresistance in magnetic multilayers, Phys. Rev. B **48**, 7099 (1993).

[61] Note that we may also be outside the weak-coupling regime that is needed for the Lindblad master equation to hold.

[62] Y. Yanay and A. A. Clerk, Reservoir engineering of bosonic lattices using chiral symmetry and localized dissipation, Phys. Rev. A **98**, 043615 (2018).

[63] X. Li, M. A. Begaowe, S. Zhang, and B. Flebus, Reciprocal reservoir induced non-Hermitian skin effect, arXiv:2307.15792.

[64] X. Zhang, T. Zhang, M.-H. Lu, and Y.-F. Chen, A review on non-Hermitian skin effect, Adv. Phys.: X **7**, 2109431 (2022).

[65] G. Wolschin, Nonlinear diffusion of fermions and bosons, Europhys. Lett. **140**, 40002 (2022).

[66] Y. Guryanova, S. Popescu, A. J. Short, R. Silva, and P. Skrzypczyk, Thermodynamics of quantum systems with multiple conserved quantities, Nat. Commun. **7**, 12049 (2016).

[67] P. N. Hai, S. Ohya, M. Tanaka, S. E. Barnes, and S. Maekawa, Electromotive force and huge magnetoresistance in magnetic tunnel junctions, Nature (London) **458**, 489 (2009).

[68] M. Bowen, Atom-level electronic physicists are needed to develop practical engines with a quantum advantage, npj Quantum Inf. **9**, 25 (2023).

[69] M. Harder, Y. Gui, and C.-M. Hu, Electrical detection of magnetization dynamics via spin rectification effects, Phys. Rep. **661**, 1 (2016).

[70] M. A. Nielsen, I. Chuang, and L. K. Grover, Quantum computation and quantum information, Am. J. Phys. **70**, 558 (2002).

[71] G. McCauley, B. Cruikshank, D. I. Bondar, and K. Jacobs, Accurate Lindblad-form master equation for weakly damped quantum systems across all regimes, npj Quantum Inf. **6**, 74 (2020).

[72] S. Braun, J. P. Ronzheimer, M. Schreiber, S. S. Hodgman, T. Rom, I. Bloch, and U. Schneider, Negative absolute temperature for motional degrees of freedom, Science **339**, 52 (2013).

[73] G. Gauthier, M. T. Reeves, X. Yu, A. S. Bradley, M. A. Baker, T. A. Bell, H. Rubinsztein-Dunlop, M. J. Davis, and T. W. Neely, Giant vortex clusters in a two-dimensional quantum fluid, Science **364**, 1264 (2019).